ChemistrySelect

Research Article
doi.org/10.1002/slct.202301173

Chemistry Europe
European Chemical
Societies Publishing

www.chemistryselect.org

In Silico Activation of CO$_2$, NO$_2$, and SO$_2$ with Light Atom Molecules and Stepwise Conversion of CO$_2$ into Methanol and Water

Stefan Mebs*[a] and Jens Beckmann[b]

CO$_2$, NO$_2$, and SO$_2$ can be activated *in silico* with tailor-made light atom tripodal ligand systems carrying particular numbers of Lewis acidic and basic sites in specific relative orientations. In the calculated EO$_2$-adducts (E=C, N, S), considerable E–O bond elongations of 0.1–0.3 Å, decreasing the E=O double bond character, and O–E–O angle alterations, approaching tetrahedral geometry, activate the donor acceptor complexes towards reduction with BH$_4^-$. The lone pairs of the P atoms thereby serve as donors towards the central element, C, N, or S, whereas the electron deficient B atoms serve as acceptors. The charge redistribution within the EO$_2$ complex was monitored by a variety of DFT-derived real-space bonding indicators (RSBIs) including bond topologies, non-covalent contact patches, and electron pair basins. For one CO$_2$-complex, the reduction towards methanol and water was conducted *via* stepwise addition of H$^-$ and H$^+$. The most critical steps are the initial CO$_2$ uptake due to potential quenching of the ligand systems in their active state, increasing the kinetic barrier, and the release of methanol and water from the ligand system due to potential ligand poisoning. Unbeneficial side reactions in the stepwise reduction and protonation have to be considered.

Introduction

Small molecule activation is at the heart of biological and chemical catalysis, the most prominent cases being presumably oxidative water splitting, nitrogen reduction, and reduction of carbon dioxide.[1–3] In nature, those complex multi-electron multi-proton tasks are conducted without exception by metal-loproteins involving base metals, such as copper, and the underlying reactions mechanisms are still under debate to date. In synthetic chemistry, heterogeneous and homogeneous catalysis typically employs the redox-properties of precious metals, such as ruthenium, rhodium and palladium,[4] but since many of these metals have a low natural abundance (and are thus expensive) and/or are harmful/toxic, transition-metal free alternatives are highly sought after. A breakthrough was achieved by Stephan and Erker in the field of homogeneous catalysis by inventing the concept of the frustrated Lewis pairs (FLPs[5–10]) around a decade ago, and particular the CO$_2$ reduction reaction (CO$_2$RR) was thoroughly investigated.[7,11,12]

With few exceptions the used FLPs were molecular pairs, means one molecule carrying a Lewis acidic (LA) site and another carrying a Lewis basic (LB) site. We are only aware of few intra-molecular FLP system which are (potentially) capable of CO$_2$RR, see scheme 1.[13–18] In the current density functional theory
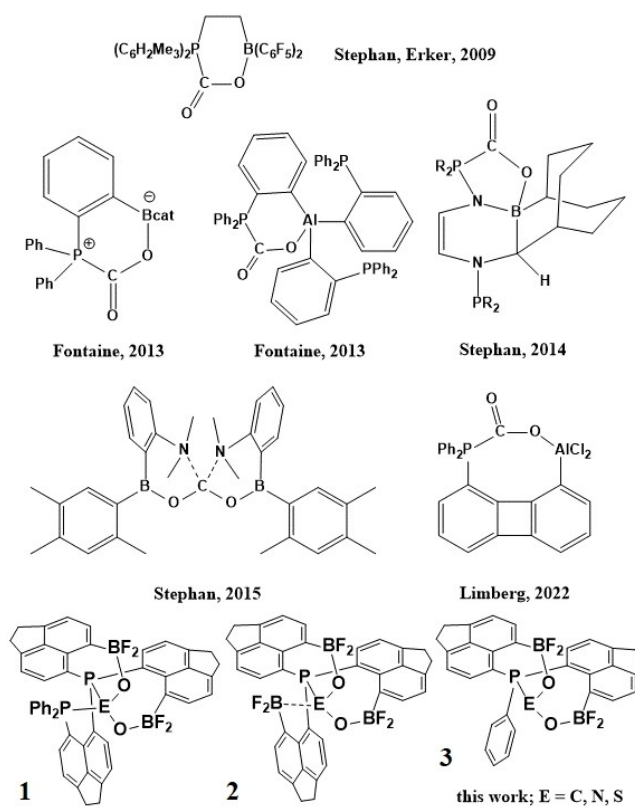
Scheme 1. Activation of CO$_2$ using intramolecular Frustrated Lewis Pairs.

[a] *Dr. S. Mebs*
Institut für Experimentalphysik, Freie Universität Berlin, Arnimallee 14, 14195 Berlin, Germany
E-mail: stefan.mebs@fu-berlin.de

[b] *Prof. Dr. J. Beckmann*
Institut für Anorganische Chemie und Kristallographie
Universität Bremen,
Leobener Straße 7, 28359 Bremen, Germany

ChemistrySelect

Research Article
doi.org/10.1002/slct.202301173

Chemistry
Europe
European Chemical
Societies Publishing

(DFT) computational study, we follow that scheme and extend the application of *intra*-molecular FLPs towards NO_2 and SO_2, both small molecules with well known noxious health and environmental properties. In a screening attempt, we employ three different *peri*-substituted scaffolds, $(6\text{-}Ph_2P\text{-}ace\text{-}5-)P(-5'\text{-}ace\text{-}6'\text{-}BF_2)_2$ (**1**), $P(-5\text{-}ace\text{-}6\text{-}BF_2)_3$ (**2**), and $PhP(-5\text{-}ace\text{-}6\text{-}BF_2)_2$ (**3**) and test their abilities to capture and activate CO_2, NO_2, and SO_2. In recent publications we showed that variations of such tripodal ligands are able to activate N_2[19,20] and capture noble gas atoms[21] and methane.[22] Crucial parameters to accomplish fixation and activation are the number and type of Lewis acidic and basic sites, and their relative orientation, respectively, as well as the size of the spacer molecule (e.g. naphthalene, acenaphthene, biphenylene, xanthene) to form frustrated Lewis pairs which do not quench *intra*-molecularly in the initial starting state. Moreover, the system needs to be flexible to accommodate for structural and electronic changes *via* the course of activation and potential chemical transformation of the target molecules, yet not too flexible, because of entropic contributions and the formation of detrimental structural isomers (rotamers). Finally, the ligand system should at least in principle be accessible by means of synthetic chemistry. The latter point dramatically reduces the otherwise overwhelmingly large number of options. The focus of this conceptual study is the impact of the number of LA and LB for a given "setup", means fixed type of LA ($-BF_2$), LB ($-PR_3$, R = *ace* or Ph), and spacer (acenaphthene, *ace*); it can be extended systematically by variation of those three fragments. An early study of 2013 by Fontaine already employed the tripodal ligand design and *peri*-substituted scaffolds, but two of the three branches were not used to activate the target molecule, so it effectively operated as single Lewis pair (scheme 1).[15] In a later study of 2015 by Stephan, two FLP-molecules contacted CO_2, effectively activating the target molecule with two acidic and two basic sites, but as trimolecular reaction.[17] Very recently, it was shown by Limberg that the single-spacer system 8-Ph_2P-*bip*-1-$AlCl_2$ (*bip* = biphenylene) is able to capture and activate CO_2.[18] We are not aware of any FLP-compound, which carries more than one (effectively operating) Lewis acidic and basic site and is employed for small molecule activation. **1** contains two LA and two LB, so we also denote it as B_2P_2 in the following. Accordingly, **2** or **3** are also denoted as B_3P or B_2P to highlight their different chemical characters. The electronic structures of the most promising model systems, in other words the most reasonable EO_2-adducts (E = C, N, S), were investigated by a set of calculated real-space bonding indicators (RSBIs), including bond topologies as well as atomic/fragmental charges using the Atoms-In-Molecules (AIM[23–25]) approach, contact patches according to the non-covalent interactions index (NCI[26]), and bonding and lone-pair basins following the electron local-izability indicator (ELI[27]) framework, all of which together provide comprehensive and complementary insight into the bond characteristics of the activated molecules. In a subsequent step, we further reduced CO_2 within the best performing CO_2-complex by adding stepwise by three hydrogen equivalents, using H^- and H^+, until the molecule formally contained the ligand system, one molecule methanol (H_3COH), and one

molecule water (H_2O), and compared the results to the ones obtained for the corresponding dicationic Si_2P_2-system, $[(6\text{-}Ph_2P\text{-}ace\text{-}5-)P(-5'\text{-}ace\text{-}6'\text{-}SiPh_2)_2]^{2+}$ (**4**), which was used for N_2 activation before,[19] see supporting information for details.

Limitations of the method. Besides the mentioned restriction to one type of Lewis acid, Lewis base, and spacer fragment, methodologic aspects such as variation of DFT functional or basis set were largely ruled out in this study; most calculations were done at one level including dispersion and solvent effects, see next section for details. Moreover, the presented CO_2 reduction pathways in the B_2P_2- and dicatonic Si_2P_2 systems to form MeOH and H_2O are limited to the lowest energy route, as most alternative routes (e.g. protonation of O instead of P or reduction of B instead of E in the early stages of the reduction) had significantly lower energy gain and/or failed to converge after extended calculation periods. Accordingly, the two proposed mechanisms rather serve as proof-of-concept than as decisive reduction pathways. Frequency calculations have been conducted for all models of the B_2P_2-, B_3P, and B_2P-systems to obtain ΔG values, however, they were discarded for the considerably larger diactionic Si_2P_2-system; for the latter, results are discussed by means of ΔE and by "penalty-corrected"-ΔG, respectively, see results section and supporting information for details.

DFT Calculations

Structural optimizations were conducted for all compounds by density functional theory (DFT) at the B3PW91/6-31+G*[28,29] level of theory using Gaussian16[30] at the curta super-computer system of the Freie Universität Berlin. Structural isomerism at each electronic state or reaction step was addressed by assigning reasonable pre-optimization structures; in case of the B_3P system this was supported by potential energy scans (PES), see below. London dispersion was modelled using Grimme's GD3BJ parameters.[31] The COSMO solvation model was applied to mimic the dichloromethane environment.[32] Normal mode (or frequency) analysis (at 298.15 K and 1 atm) proved the relaxed geometries to be local minima on the potential energy hypersurface and provided ΔG values, which were corrected for basis-set superposition errors (BSSE) as well as for the 1 atm to 1 M conversion. The BSSE was estimated using the counter-poise correction method in Gaussian16 by fragmentation of the EO_2-complexes into EO_2-guest and ligand host; the conversion from the 1 atm standard state (ΔG°_{atm}) to the 1 M standard state (ΔG°_M) was conducted according to $\Delta G^{\circ}_M = \Delta G^{\circ}_{atm} + R_1T \ln(R_2 T^{\Delta n})$ with $R_1 = 8.31447\ J\,K^{-1}\,mol^{-1}$, $R_2 = 0.08206\ L\,atm\,K^{-1}\,mol^{-1}$, T = temperature in K, and n = change in number of moles, causing a free enthalpy expense of $7.9\ kJ\,mol^{-1}$.[33] The $-Ph_2P\cdots BF_2-$ *peri*-interaction energy (α-PIE) was estimated twofold, using a potential energy scan with fixed $P\cdots B$-distances of 2.50, 2.75, and 3.00 Å, as well as by the *isodesmic* approach, comparing the energy sum of the optimized di-substituted system 5-Ph_2P-*ace*-6-BF_2 and non-substituted acenaphthene with the two different mon-sub-stituted model systems, i.e. X-spacer-Y + spacer vs. X-spacer + spacer-Y (X, Y: substituents). PES were also employed to

ChemistrySelect

Research Article
doi.org/10.1002/slct.202301173

Chemistry
Europe

European Chemical
Societies Publishing

estimate the rotational barrier of the B_3P ligand system (fixed C_π–C_π–P–C_π or C_π–C_π–C_π–C_π torsion angles), the EO_2-entrance barriers (fixed P···E distances) as well as the barriers of adding hydride for CO_2-reduction (fixed C···H$^-$ distances); or adding protons for charge compensation (fixed C···H$^+$ distances) In addition, transition-states for EO_2-uptake to form the three relevant EO_2-complexes were calculated using the PES-maxima as starting coordinates and applying the Berny algorithm as implemented in Gaussian 16. Normal mode analysis of the transition-states revealed the existence of one negative frequency each (TS–CO_2: -151.9 cm^{-1}, TS–NO_2: -188.1 cm^{-1}, TS–SO_2: -33.3 cm^{-1}) reflecting the motion of EO_2 towards the central P atom (NO_2, SO_2) or the *peri* P atom (CO_2). The electronic structure of relevant EO_2-complexes was extracted from the calculated electron and electron pair densities according to the following methods: a topological analysis of the electron density (ED, Atoms-In-Molecules – AIM[23–25] approach) applying AIM2000,[34] bonding and lone-pair basin analysis (Electron-Localizability-Indicator – ELI-D[27] approach) applying DGRID-5-1[35] (grid step size: 0.05 a.u.), *intra*-molecular contact patches (non-covalent interactions index – NCI[26] approach) applying NCIplot[36] (grid step size: 0.07 a.u.). Analyses of the reduced density gradient, $s(r) = [1/2(3\pi^2)^{1/3}] |\nabla\varrho| / \varrho^{4/3}$, according to the NCI method is used to visualize non-covalent bonding aspects. An estimation of different non-covalent contact types according to steric/repulsive ($\lambda_2 > 0$, red-colored), van der Waals-like ($\lambda_2 \approx 0$, green-colored), and attractive ($\lambda_2 < 0$, blue-colored) is facilitated by mapping the ED times the sign of the second eigenvalue of the Hessian (sign(λ_2)ϱ) on the *iso*-surfaces of $s(r)$. For ELI–D figures, additional grids of 0.12 or 0.15 a.u. step size were computed. Structures are displayed with GaussView, bond paths are displayed with AIM2000, NCI and ELI–D figures are displayed with Mollso.[37] Frontier orbitals were evaluated for the CO_2-complex. The steady-state structures of the CO_2-reduction pathway were reoptimized at the higher B3PW91/6-311+G(2df,p) level of theory, fully resembling the trends obtained for the lower-level calculations.

Results and discussion

Structures and energies. To be operational against small molecule activation, the three *peri*-substituted scaffolds, (6-Ph$_2$P-*ace*-5–)P($-6'$-*ace*-5'-BF$_2$)$_2$ (**1**, B_2P_2), P(-6-*ace*-5-BF$_2$)$_3$ (**2**, B_3P), and PhP(-5-*ace*-6-BF$_2$)$_2$ (**3**, B_2P) have to be oriented in the right way, forming the crucial binding pocket or active site ("active state"). Accordingly, conformational isomers in which the Lewis acidic and basic sites are considerably quenching each other ("quench state") or are located far away from each other ("dead state") have to be ruled out. Figure 1 displays the active conformers of the three ligand systems, Figure S1 displays unfavorable counterparts. For the B_2P_2-system, the active state is 40.2 kJ mol^{-1} lower in energy than the dead state, making it the main reaction product. However, the less steric crowded system B_3P shows slight preference for a rather quenched state (d(B,P) = 2.090 Å, $\Delta E = -14.0$ kJ mol^{-1}) and the dead state ($\Delta E = -25.5$ kJ mol^{-1}), whereas both products (active and dead) are basically equally stable for the smallest ligand,
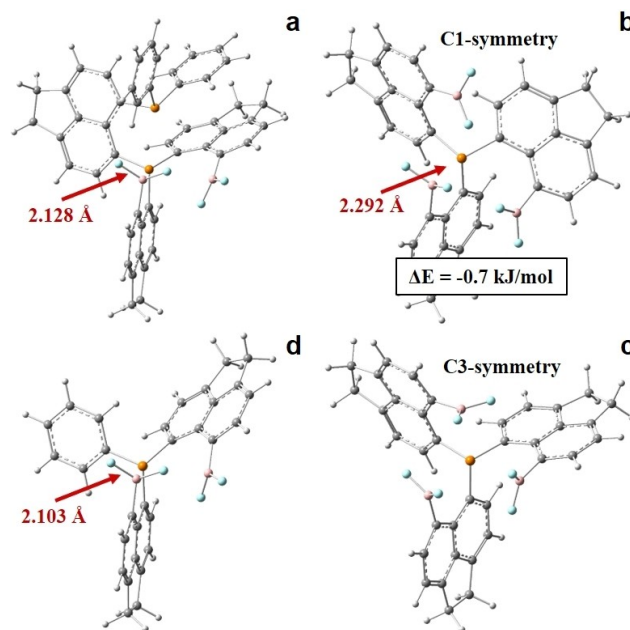
Figure 1. Ligand systems investigated for uptake and activation of CO_2, NO_2, and SO_2: a) (6-Ph$_2$P-*ace*-5–)P(-5-*ace*-BF$_2$)$_2$ (**1**); b) P(-5-*ace*-BF$_2$)$_3$ in the asymmetric (**2-C1**) form; P(-5-*ace*-BF$_2$)$_3$ in the symmetric (**2-C3**) form; d) PhP(-5-*ace*-BF$_2$)$_2$ (**3**).

B_2P ($\Delta E = 2.3$ kJ mol^{-1}). In order to estimate the rotational barriers within the B_3P system, potential energy scans (PES) with fixed C_π–C_π–P–C_π or C_π–C_π–C_π–C_π torsion angles were conducted (Figure S2), never exceeding 38 kJ mol^{-1}, suggesting one the one hand a complex rotational hypersurface but on the other hand easy accessibility of the active isomer(s) under ambient conditions. Moreover, if one considers ΔG instead of ΔE, the difference between active and dead isomer of B_3P drops down to -13.9 kJ mol^{-1} due to less degrees of freedom in the dead-end state. Even lower activation barriers for rotational isomerism are expected for B_2P. Notably, for B_3P, two equally stable active state conformations were found, an asymmetric one (C1-symmetry) and one approaching C3-symmetry following the threefold ligand design. This may become relevant, because in the C1-variant, a short P–B contact of about 2.3 Å is formed, potentially hampering uptake of the EO_2 (E=C, N, S) target molecules, whereas all three B atoms are about 3 Å away from the central P atom in the variant approaching C3-symmetry. Similar short P–B distances of 2.128 Å (B_2P_2) and 2.103 Å (B_2P) rise the question about the strength of these interactions. As an estimate, the *peri*-interaction energy (PIE) of the simple model 5-Ph$_2$P-*ace*-6-BF$_2$ was calculated by the isodesmic approach (see methods section and Figure S3 in the supporting information; α-PIE) and additionally by a potential energy scan (PES), i.e. by stretching the B–P bond systematically. The isodesmic approach proposes an α-PIE of -18.0 kJ mol^{-1}, whereas the PES finds a value of -35.3 kJ mol^{-1}. The smaller value of the α-PIE can be explained by the misleading energetic effect of secondary –B(F)F···H and –Ph$_2$P···H interactions in the mono-substituted complexes (see

ChemistrySelect

Research Article
doi.org/10.1002/slct.202301173

Chemistry Europe
European Chemical
Societies Publishing

supporting information for details), thus the PES-results are considered to be more reliable. However, even with -35.3 kJ mol^{-1}, the B–P contact strength is not large enough to prohibit EO$_2$ uptake. As shown in the recently published 1-Ph$_2$P-*bip*-8-AlCl$_2$ case, even the estimated α-PIE of -84.9 kJ mol^{-1} couldn't prevent CO$_2$ uptake at an CO$_2$ pressure

of 2 bar.[18] Accordingly, we propose all four models shown in Figure 1 to be potentially active against EO$_2$ uptake.

The three ligand systems, **1**–**3**, were tested against uptake of CO$_2$, NO$_2$, and SO$_2$, resulting in nine EO$_2$-complexes, see Tables 1 and 2 for relevant geometric parameters and energetic/enthaplic values as well as Figure 2 for structural representations of the three most promising candidates, **1-CO$_2$**,

Table 1. Relevant bond distances and angles in the EO$_2$-adducts, relevant transition states, and the respective reduced states.

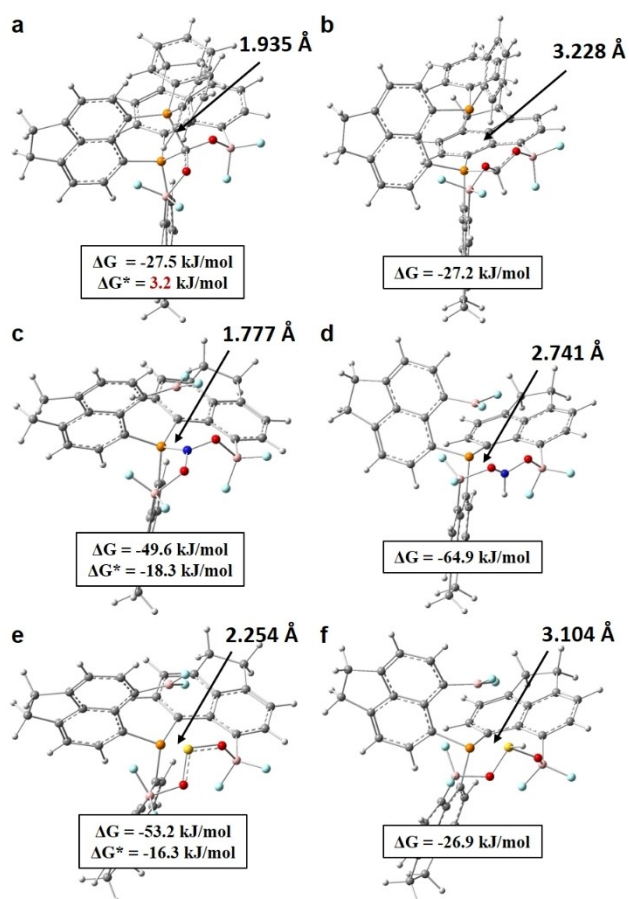| B$_2$P$_2$ (1)	d$_{(E-O1)}$	d$_{(E-O2)}$	d$_{(E-Pc)}$	d$_{(E-Pl)}$	d$_{(O1-B)}$	d$_{(O2-B)}$	O-E-O	d$_{(E-H)}$	Δ(E-O1)	Δ(E-O2)	Δ(OEO)
TS-CO$_2$	1.197	1.206	*3.122*	2.272	3.240	2.494	147.7		0.030	0.039	−32.3
CO$_2$	1.343	1.353	1.890	1.935	1.490	1.496	112.0		0.175	0.186	−68.0
CO$_2$-red	1.354	1.344	1.971	*3.228*	1.476	1.477	113.0	1.096	0.187	0.176	−67.0
NO$_2$	1.311	1.320	1.790	*2.801*	1.311	1.320	112.7		0.115	0.124	−21.5
NO$_2$-red	1.360	1.346	*2.474*	*3.211*	1.510	1.514	111.7	1.026	0.164	0.149	−22.5
SO$_2$	1.804	1.726	2.190	2.179	1.442	1.466			0.341	0.263	
SO$_2$-red	*3.312*	1.667	*4.327*	*3.584*	1.519	1.480		1.351	*1.849*	0.205	

B$_3$P (2)	d$_{(E-O1)}$	d$_{(E-O2)}$	d$_{(E-Pc)}$	d$_{(E-B)}$	d$_{(O1-B)}$	d$_{(O2-B)}$	O-E-O	d$_{(E-H)}$	Δ(E-O1)	Δ(E-O2)	Δ(OEO)
CO$_2$	1.249	1.261	1.872	*3.078*	1.605	1.617	121.4		0.082	0.094	−58.6
CO$_2$-red-v1	1.347	1.415	1.866	*2.622*	1.482	1.571	111.1	1.097	0.179	0.248	−68.9
CO$_2$-red-v2	1.361	1.358	1.940	*3.140*	1.472	1.484	114.5	1.097	0.193	0.190	−65.5
TS-NO$_2$	1.321	1.236	2.302	1.753	1.531	*2.638*	118.7		0.125	0.040	−15.5
NO$_2$	1.299	1.313	1.777	*3.445*	1.595	1.595	115.0		0.102	0.117	−19.2
NO$_2$-red-v1	1.302	1.299	1.781	*3.343*	1.577	1.577	115.8	2.273	0.106	0.103	−18.5
NO$_2$-red-v2	1.309	1.306	*2.741*	*3.668*	1.560	1.565	116.8	1.028	0.113	0.110	−17.5
TS-SO$_2$	1.468	1.469	*3.325*	*3.704*	*3.845*	*2.952*	116.1		0.005	0.006	−1.4
SO$_2$	1.564	1.543	2.254	*2.955*	1.564	1.590	106.7		0.101	0.080	−10.8
SO$_2$-red-v1	1.576	1.572	*3.104*	*3.368*	1.548	1.556	105.6	1.368	0.113	0.109	−11.8
SO2-red-v2	1.641	1.645	*3.554*	*4.409*	1.496	1.489	106.1	2.142	0.178	0.182	−11.3

B$_2$P (3)	d$_{(E-O1)}$	d$_{(E-O2)}$	d$_{(E-Pc)}$		d$_{(O1-B)}$	d$_{(O2-B)}$	O-E-O	d$_{(E-H)}$	Δ(E-O1)	Δ(E-O2)	Δ(OEO)
CO$_2$	1.252	1.258	1.878		1.600	1.592	120.7		0.084	0.091	−59.3
CO$_2$-red-v1	1.363	1.358	1.939		1.470	1.481	113.6	1.100	0.196	0.190	−66.4
CO$_2$-red-v2	1.360	1.358	1.922		1.466	1.480	112.4	1.099	0.192	0.191	−67.6
NO$_2$	1.301	1.311	1.780		1.588	1.595	115.0		0.104	0.115	−19.3
NO$_2$-red-v1	1.356	1.338	*2.526*		1.519	1.529	112.8	1.021	0.159	0.141	−21.5
NO$_2$-red-v2	1.358	1.353	*2.332*		1.510	1.491	110.3	1.031	0.162	0.157	−23.9
SO$_2$	1.569	1.546	2.251		1.560	1.589	106.2		0.106	0.083	−11.3
SO$_2$-red-v1	1.580	1.574	*2.967*		1.542	1.549	105.1	1.371	0.117	0.111	−12.4
SO$_2$-red-v2	1.666	1.632	*3.490*		1.476	1.493	100.6	2.118	0.203	0.169	−16.9

Δ-values compare the EO$_2$-fragments in the adducts with the gaseous EO$_2$ molecules. For clarity, atom-atom contact distances larger than 2.3 Å are given in italic. Calculated reference distances and angles of the gaseous EO$_2$ molecules are: CO$_2$—d$_{(C-O)}$ = 1.167 Å, O–C–O = 180°; NO$_2$—d$_{(N-O)}$ = 1.196 Å, O–N–O = 134.2°; SO$_2$—d$_{(S-O)}$ = 1.463 Å, O–S–O = 117.5°.

Table 2. Adduct formation energies and free enthalpies (in kJ mol^{-1}).[$]

	1 (B$_2$P$_2$)			2 (B$_3$P)			3 (B$_2$P)		
	CO$_2$	NO$_2$	SO$_2$	CO$_2$	NO$_2$	SO$_2$	CO$_2$	NO$_2$	SO$_2$
ΔE	−96.3	−101.9	−43.6	−45.8	−116.6	−125.0	−37.0	−103.7	−118.0
ΔG	−27.5	−38.0	31.8	*15.3*	−49.6	−53.2	*23.4*	−36.3	−48.0
BSSE	22.8	23.8	34.0	18.2	23.4	29.0	16.4	21.0	27.6
ΔG′	−4.7	−14.3	65.8	33.6	−26.2	−24.2	*39.8*	−15.3	−20.4
ΔG″	*3.2*	−6.4	73.7	*41.5*	−18.3	−16.3	*47.7*	−7.4	−12.5
Δ(ΔG″-ΔE)	99.5	95.5	117.4	87.2	98.2	108.7	84.7	96.3	105.5
ΔG-red-v1	−27.2	−54.1	−272.5	−131.7	*5.0*	−26.9	−96.6	−50.0	−19.2
ΔG-red-v2				−87.8	−64.9	−79.2	−88.1	−41.0	−62.8

[$] Values compare adducts with the "active states", **1**–**3**; for B$_3$P, the dead-end-state is 25.5 kJ mol^{-1} lower in energy. ΔG′ is the BSSE-corrected ΔG; ΔG″ is ΔG′ corrected for the 1 atm to 1 M conversion ($+7.9$ kJ mol^{-1}).

ChemistrySelect

Research Article
doi.org/10.1002/slct.202301173

Chemistry
Europe
European Chemical
Societies Publishing

Figure 2. (a, c, e) Exemplary EO_2-adducts and corresponding first reduction steps with H^- (b, d, f). For CO_2, the B_2P_2-ligand (1) is shown (a and b), whereas the B_3P-ligand (2) is shown for NO_2 (c and d) and SO_2 (e and f).

2-NO_2, and **2-SO_2**. Two types of kinetic barriers were considered by means of potential energy scans (PES) as well as transition-state (TS) calculations for **1-CO_2**, **2-NO_2**, and **2-SO_2**, which may hamper EO_2-complex formation although the complexes being thermodynamically favored over the educts: An external barrier ("EO_2-entry barrier") and an internal barrier ("EO_2-deformation barrier"), see Figure S4. Weak secondary interactions (e.g. dispersion) initiate molecular assembly of EO_2 and ligand system (energetic decrease between 10 and about 5 Å E···P distance, Figure S4a). When the EO_2 molecule approaches the active site its O atoms will be attracted by the electron deficient B atoms (in case of CO_2 and NO_2), whereas the positively charges E atoms will be attracted by the lone pairs of the P atoms (in case of CO_2 and NO_2) and/or of the F atoms (in case of SO_2), however, the non-bonding electron in NO_2 also attracts an adjacent B atom; all effects together causing EO_2 activation. "Opening" the partially quenched active site to embed EO_2 then requires energy (energetic increase between about 5 Å and the TS-structures **TS-1-CO_2**, **TS-2-NO_2**, and **TS-2-SO_2**). The overall entry barrier of CO_2 is estimated to be 68 kJ mol^{-1}, whereas considerably smaller barriers were obtained for NO_2 and SO_2, which means EO_2-uptake would take place under ambient conditions for the latter two cases, whereas CO_2-uptake likely requires application of enhanced CO_2-pressure. CO_2 and particularly SO_2 show early (educt-like) transitions states for EO_2-complex formation, whereas NO_2 shows a late (product-like) TS, see Table 1 and Figure S4. This is also reflected in the respective ligand-strain (23.4 kJ mol^{-1} for **TS-2-SO_2**, 69.7 kJ mol^{-1} for **TS-1-CO_2**, 251.8 kJ mol^{-1} for **TS-2-NO_2**), which was estimated by extraction of the EO_2-fragment from the three TS-structures and subsequent single-point calculation on the empty ligand system fixed in the TS-geometry. As EO_2-entry into the flexible ligand systems is complex, it can't be fully excluded that there are other transition states characterizing slightly different entry channels. However, once being embedded within the active site, all three EO_2 molecules are bent towards close-to-tetrahedral angles (Figure S4b) and the E–O bonds are stretched without any further barrier, which is thoroughly explained by the electric field being exerted to the target molecule by the frustrated Lewis pair(s). Similar observations have been made for H_2[9] and N_2[19,20] before. In the EO_2-complexes, the ligand strain rises to 380.8 kJ mol^{-1} for **1-CO_2** and 280.7 kJ mol^{-1} for **2-SO_2**, but remains almost unchanged at 251.2 kJ mol^{-1} for **2-NO_2**. Those large numbers are due to backbone bending, reorganization of the $-BF_2$ fragments, and lost P–B and F–B interactions. Single-point calculations on the cut-out activated EO_2-fragments revealed a drastic strain of 483.4 kJ mol^{-1} for CO_2, considerably smaller 109.5 kJ mol^{-1} for SO_2, and minor 52.0 kJ mol^{-1} for NO_2. The high energy expenses of ligand and EO_2 deformation within the complexes apparently has to be overcompensated by the complex formation energy which is mainly comprised of strong P–E and O–B polar-covalent interactions but also includes dispersive interactions.

In order to understand if the bound and activated EO_2-fragments are prone to reduction and thus chemical conversion towards value added species, hydride, H^-, was added to the complexes, see Figures S5–9 for all models. As structural isomerism has to be considered in every step, two variants (red-v1 and red-v2) were calculated for the smaller ligand systems **2** and **3**.

All EO_2-complexes exhibit the same binding mode, that is the P atom(s) of the ligand systems donate into the central C, N, or S atom, whereas the two O atoms of the EO_2-molecule donate into the B atoms of the adjacent $-BF_2$ fragments, see Figure 2 for representative examples and Figures S5–9. This causes considerable E–O bond elongations of 0.1 to 0.3 Å (Table 1). There is a trend towards stronger E–O bond activation for the B_2P_2-system (**1**) compared to the ligands carrying only one P atom (**2**, **3**). Similar results are obtained for B_3P- and B_2P-systems, hinting towards a negligible role of the third $-BF_2$ fragment, which is in loose contact with the central C, N, or S atom. More remarkable than the E–O bond elongations are the significant alterations of the O–E–O angles, which are as high as 60–70° for CO_2, about 20° for NO_2, and about 10° for SO_2, ultimately approaching tetrahedral "sp³-like" local geometries around the central E atoms with O–E–O angles of 106–121°. This pre-organization of the target molecules within the ligand hosts is somewhat reminiscent to

ChemistrySelect

Research Article
doi.org/10.1002/slct.202301173

Chemistry Europe
European Chemical
Societies Publishing

the entatic state principle in proteins activating substrate molecules.[38] The energies and free enthalpies of the complex formation process of all nine cases are given in Table 2. The simple energy sum difference of the adduct vs. the free ligand and EO_2 molecule (ΔE) suggests all combinations to be potential candidates for EO_2-activation, however, the subsequently extracted free enthalpies (ΔG) hint towards an endothermic CO_2-adduct formation process for the smaller ligands **2** and **3**, carrying only one Lewis basic $-PPh_2$ site, highlighting the role of the latter. This situation becomes even more unfortunate after correction for the basis-set superposition error (BSSE; $\Delta G'$), the noncompliance of which can lead to erroneously strong adduct formation energies/enthalpies. Finally, since gaseous EO_2 is solvated into the solution containing the ligand system, the conversion form 1 atm to 1 M has to be conducted, adding another 7.9 kJ mol^{-1} to the enthalpy ($\Delta G''$).[33] The overall change from ΔE to $\Delta G''$ sums up to remarkable 85–117 kJ mol^{-1}, so an estimate of $+100$ kJ mol^{-1} as a "penalty" seems to be suitable if systems have to be judged on the basic ΔE-level as frequency calculations are not affordable due to the size of the investigated systems. However, it should also be noted that there are indications for overestimation of entropic terms in DFT,[39,40] and that the BSSE-calculations for technical reasons don't include the COSMO solvation model, highlighting the fact that also $\Delta G''$ is an estimate, and that small positive $\Delta G''$ numbers are no fundamental flaw for adduct formation in the laboratory. This is exemplified by the recently published 1-Ph$_2$P-*bip*-8-AlCl$_2$ case, which has a negative adduct formation energy ($\Delta E =$ -57.8 kJ mol^{-1}) on the here applied DFT-level, a slightly negative free enthalpy ($\Delta G = -4.1$ kJ mol^{-1}), which, after BSSE-correction (12.4 kJ mol^{-1}) and 1 atm to 1 M correction (7.9 kJ mol^{-1}) turns slightly positive ($\Delta G'' = 16.2$ kJ mol^{-1}), yet it was formed synthetically by applying a CO_2-pressure of 2 bar.[18]

Notably, for NO_2 and SO_2 the B_2P_2-ligand shows inferior results compared to the smaller ligand systems, pointing towards an unfavorable effect of the second P atom, the lone-pair of which likely interferes with the non-bonding electron(s) located at the central N or S atoms. In contrast, a moderate but improving effect towards adduct stabilization was obtained by the third Lewis acidic $-BF_2$ site in **2** compared to ligand system **3**, see Table 2. For all nine cases, however, reduction by adding hydride is strongly favored, which in most cases caused the breaking of a P–E or B–E bond, see italic-style distance numbers in Table 1. Thus, from an energetic/enthalpic, kinetic, and structural point of view, the proposed bipodal (B_2P) or tripodal (B_3P, B_2P_2) ligand systems are capable of uptake and activation of small EO_2 molecules such as CO_2, NO_2, and SO_2 by forcing them into an "entatic-state-like" environment. Activation of small molecules by FLPs is possible as the latter exert an electric field on the former, which was analyzed in great detail for H_2 in an early FLP-study;[9] for bond activation with FLPs, see also reference [5], which shows how initial frustration of the ligand system rises its molecular energy, thereby decreasing the kinetic barrier of complex formation (H_2 in this case). Variation of solvent, Lewis acidic and basic sites as well as of

the spacer fragments likely further improves these features towards energy efficient EO_2-complex formation.

Real-space bonding indicator analysis. The electronic structure of the most promising donor-acceptor complexes, **1-CO$_2$**, **2-NO$_2$**, and **2-SO$_2$** (parts a, c, and e in Figure 2) was thoroughly investigated by employing the calculated electron and electron pair densities according to the AIM,[23–25] NCI,[26] and ELI-D[27] toolkits, with a focus on the stretched E–O bonds. Topological and integrated C–O bond descriptors are collected in Table 3, whereas Table 4 displays AIM atomic and fragmental charges comparing the free EO_2 and ligand molecules with the EO_2-adducts. RSBI of the O–B and P–B bonds and of lone-pairs basins are collected in Table S7. C=O, N=O, and S=O are all strongly polarized covalent bonds with significant covalent and ionic bond contributions. Accordingly, these bonds are short and strong, which is reflected in electron density (ED, $\varrho(\mathbf{r})_{bcp}$) values of 3.0, 3.5, and 1.9 eÅ^{-3} at the respective bond critical points (bcps) and strong electron populations in the corresponding ELI–D bonding basins (N_{ELI}) of 2.8, 3.4, and 3.0 e in the gaseous EO_2 molecules. For the C=O bonds of CO_2, ionic contributions are slightly dominant according to AIM, which is reflected by the fact that the modulus of the kinetic energy density over ED ratio, $G/\varrho(\mathbf{r})_{bcp}$, is slightly larger than the modulus of the total energy density over ED ratio, $H/\varrho(\mathbf{r})_{bcp}$. The Raub-Jansen-Index (RJI[41]), which dissects ELI–D basins and quantifies the contributions of adjacent AIM atomic basins to that ELI–D basin, and is thus a measure for bond polarity, is 71%, a typical value for polar-covalent interactions. A much stronger ionic prevalence is obtained for the S=O bonds in SO_2,[42] causing a considerable positive Laplacian of the ED, $\nabla^2\varrho(\mathbf{r})_{bcp}$, and a RJI of 80%. To the opposite, clear prevalence of covalent bonding aspects is observed for the N=O bonds in NO_2, resulting in a strongly negative Laplacian and a RJI of close to 50%. Figure S10 shows the AIM topology and ELI–D localization domain representation of CO_2, NO_2, and SO_2. Linear CO_2 has two types of valence basins, C=O bonding as well as toroidal oxygen lone-pair basins (LP(O)), whereas the tilted radical NO_2 as well as SO_2 exhibit four basin types, E=O bonding, LP(E), and two LP(O)s.

The electronic situation of the E=O bonds changes drastically *via* complex formation. Figures 3, 4 and S11 display AIM-topologies, NCI contact patterns, and ELI–D representations of **1-CO$_2$**, **2-NO$_2$**, and **2-SO$_2$**; the AIM-topologies of the three EO_2-complex formation transition-states are displayed in Figure S16. In the 0.1–0.3 Å elongated E–O bonds within the EO_2-complexes, the ED at the bcp drops down by 0.2–0.9 eÅ^{-3}, and N_{ELI} drops down by astonishing 1.4–2.2 e, accompanied by decreased basin volumes (V_{ELI}). Notably, in case of CO_2 and SO_2, the E=O bonds of which are dominated by ionic contributions in the free EO_2 molecules, the bond weakening goes mainly to the expense of ionic aspects, as reflected in decreased RJI values, in an inverted energy density ratio ($G/\varrho(\mathbf{r})_{bcp} < |H/\varrho(\mathbf{r})_{bcp}|$) for CO_2, turning also the sign of the Laplacian, and a much smaller difference between the energy densities for SO_2, bringing the formerly strongly positive Laplacian much closer to zero. The anyways covalently dominated N=O bonds, to the contrast, become also weaker, but keep their general bonding

ChemistrySelect

Research Article
doi.org/10.1002/slct.202301173

Chemistry Europe
European Chemical
Societies Publishing

Table 3. Topological and integrated AIM and ELI bonding indicators of the E–O bonds.

model	contact	d [Å]	d_1/d	$\varrho(r)_{bcp}$ [e$Å^{-3}$]	$\nabla^2\varrho(r)_{bcp}$ [e$Å^{-5}$]	ε
CO_2	C–O	1.167	0.66	3.00	11.5	0.00
1-CO_2	C–O1	1.343	0.66	2.08	−13.1	0.10
1-CO_2	C–O2	1.353	0.66	2.06	−15.5	0.06
NO_2	N–O	1.196	0.54	3.51	−27.5	0.06
2-NO_2	N–O1	1.299	0.53	2.75	−17.1	0.15
2-NO_2	N–O2	1.313	0.52	2.68	−15.8	0.06
SO_2	S–O	1.463	0.61	1.86	30.2	0.15
2-SO_2	S–O1	1.564	0.61	1.59	7.4	0.22
2-SO_2	S–O2	1.543	0.61	1.62	11.4	0.10

contact	$G/\varrho(r)_{bcp}$ [a.u.]	$H/\varrho(r)_{bcp}$ [a.u.]	N_{ELI} [e]	V_{ELI} [$Å^3$]	γ_{ELI}	RJI [%]
C–O	2.00	−1.73	2.79	6.8	1.426	71.0
C–O1	1.14	−1.58	1.41	1.2	1.566	75.5
C–O2	1.05	−1.57	1.40	1.2	1.578	73.8
N–O	0.83	−1.38	3.39	2.4	1.605	44.8
N–O1	0.68	−1.12	1.16	0.6	1.614	51.5
N–O2	0.67	−1.08	1.15	0.7	1.629	43.5
S–O	2.22	−1.08	3.03	3.0	1.403	79.6
S–O1	1.48	−1.15	1.15	1.1	1.441	73.5
S–O2	1.63	−1.14	1.25	1.3	1.449	71.8

$\varrho(r)_{bcp}$: ED at the bcp, $\nabla^2\varrho(r)_{bcp}$: Laplacian, ε: bond ellipticity d_1: distance atom(1)-bcp, $G/\varrho(r)_{bcp}$, $H/\varrho(r)_{bcp}$: kinetic and total energy density over $\varrho(r)_{bcp}$ ratios, N_{ELI}, V_{ELI}: electron populations and volumes the ELI–D basin, γ_{ELI}: ELI–D value at the attractor position, RJI: Raub-Jansen Index.
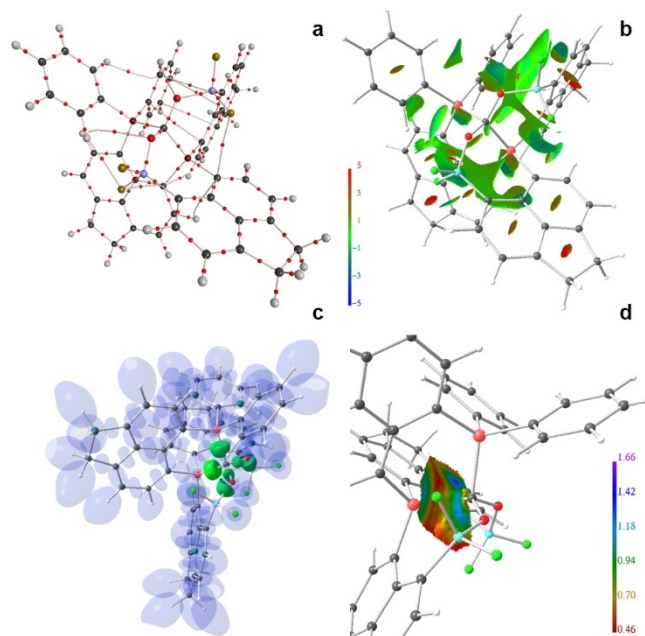
Table 4. AIM atomic and fragmental charges (in e).

	CO_2+1	1-CO_2	Δ		NO_2+2	2-NO_2	Δ	SO_2+2	2-SO_2	Δ
C	2.33	0.66	−1.67	E	0.72	−0.07	−0.79	2.37	1.60	−0.77
O	−1.15	−1.31	−0.16	O	−0.34	−0.67	−0.33	−1.16	−1.29	−0.13
O	−1.15	−1.31	−0.16	O	−0.34	−0.74	−0.40	−1.16	−1.30	−0.13
CO_2	0.03	−1.96	−1.99	EO_2	0.04	−1.48	−1.52	0.05	−0.98	−1.03
P	1.72	2.52	0.79	P	1.64	2.83	1.18	1.64	2.19	0.54
BF_2(1)	0.61	0.59	−0.02	BF_2(1)	0.60	0.60	0.00	0.60	0.59	−0.01
BF_2(2)[$]	0.35	0.57	0.22	BF_2(2)	0.60	0.58	−0.02	0.60	0.59	−0.02
PPh_2	0.63	1.49	0.85	BF_2(3)	0.60	0.62	0.02	0.60	0.60	0.00
ace(1)	−0.99	−0.92	0.07	ace(1)	−1.10	−0.98	0.11	−1.10	−0.97	0.13
ace(2)	−1.08	−1.11	−0.03	ace(2)	−1.12	−1.04	0.08	−1.12	−1.02	0.10
ace(3)	−1.17	−1.10	0.07	ace(3)	−1.12	−1.03	0.09	−1.12	−1.02	0.10
Σ	0.11	0.07		Σ	0.15	0.08		0.16	−0.02	

[$] This BF_2 group is involved in a short F_2B–PPh_2 contact in the free ligand.

characteristics. The slightly increased bond ellipticities, ε, indicate minor distortions from the cylindrical shape of the ED along the E–O axes. Slightly larger values for the electron localizability at the ELI–D basin attractor positions, γ_{ELI}, go in line with higher covalent bonding aspects in localized covalent bonds. Drastic changes, however, are not only observed for the E–O bond properties, but also for the atomic and fragmental AIM charges, see Table 4. The EO_2-fragments within the EO_2-complexes are reduced by about 2e (CO_2), 1.5 e (NO_2), and 1.0 e (SO_2) with respect to their unbound counterparts, the majority of which accumulates at the central E atom (−1.7 e in CO_2, −0.8 e in NO_2 or SO_2); 0.1–0.4 e are located at the O atoms. Equally strong charge accumulation effects have been obtained in the recently published works on N_2-activation with related ligand molecules.[19,20] The vast majority of this charge stems

from the P atoms lone pairs, LP(P), of the ligand molecules, minor contributions come from the acenaphthene backbones. Surprisingly, the −BF_2 fragments, although being involved in polar-covalent O–B bonds in the adducts, show negligible changes. One exception is the −BF_2 fragment which is involved in a P–B already in the free B_2P_2 ligand (**1**). One might expect that the negative charge in the activated EO_2 (or N_2) fragments facilitate subsequent protonation at the central atom, but it turned out for EO_2 (as well as for N_2 in the two previous studies) that contrariwise chemical reduction with hydride is strongly favored, see next section for details. The AIM bond topologies and NCI contact patterns show only few secondary interactions between the EO_2 fragments and the hosting ligand molecules (parts a and b of Figures 3, 4 and S11). In **2-NO₂** and **2-SO₂**, the third −BF_2 fragment being not involved in a O–B bond is just

ChemistrySelect

Research Article
doi.org/10.1002/slct.202301173
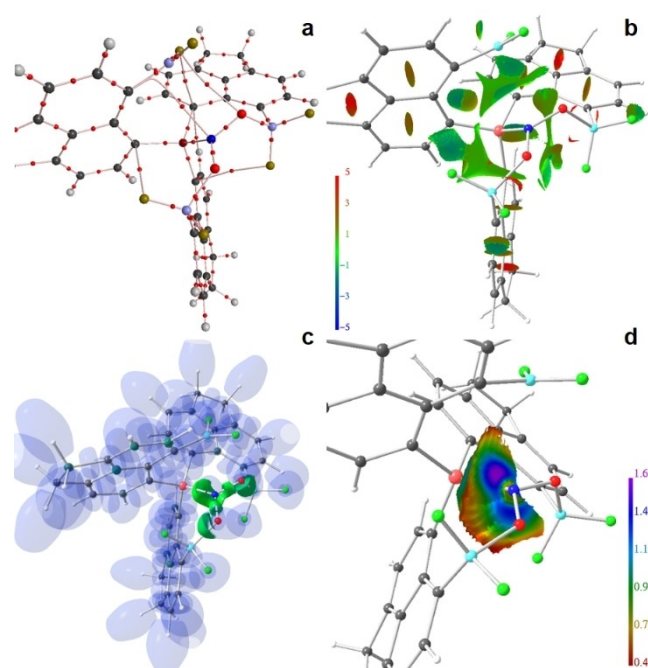
Chemistry Europe
European Chemical
Societies Publishing

Figure 3. RSBI analysis of **1-CO$_2$** (a) AIM bond paths motif, (b) NCI iso-surface at s(r) = 0.5, (c) ELI–D localization domain representation at iso-value of 1.4, (d) ELI–D distribution mapped on the P–CO$_2$ ELI–D bonding basin. Color code atoms: hydrogen – light gray, carbon – medium gray, oxygen – medium red, phosphor – dark or pale red, fluorine – green or brown, boron – light blue.

Figure 4. RSBI analysis of **2-NO$_2$** (a) AIM bond paths motif, (b) NCI iso-surface at s(r) = 0.5, (c) ELI–D localization domain representation at iso-value of 1.4, (d) ELI–D distribution mapped on the P–CO$_2$ ELI–D bonding basin. Color code atoms: hydrogen – light gray, carbon – medium gray, oxygen – medium red, nitrogen – blue, phosphor – dark or pale red, fluorine – green or brown, boron – light blue.
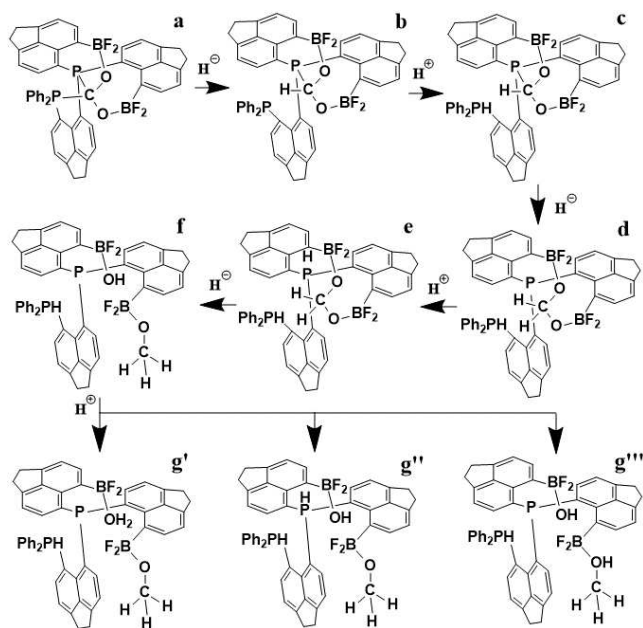
loosely connected to the central E atom by Van-der-Waals like interactions, which is reflected in the formation of a large and flat, greenish-colored NCI-basin between the BF$_2$- and EO$_2$-fragments, so it might be considered as dispensable, however, it's main purpose is the prevention of quenching of the ligand molecule by forming a short P–B bond (although it was found that this issue is not so critical, see upper section). At an ELI–D value of 1.4, the P–C and C–O bonding basins in **1-CO$_2$** are clearly separated (Figure 3c), whereas P–C and N–O are still topologically fused in **2-NO$_2$** (Figure 4c), indicating a higher degree of activation in the former. Accordingly, lower localizability values are seen on the P–C basin surface of **1-CO$_2$** (Figure 3d) in direction towards the O atoms compared to the corresponding P–N basin surface of **2-NO$_2$** (Figure 4d).

The contact between the C, N, or S atom and the central P atom is already topologically established in the transition states (Figures S16) for P···E distances of 3.122 Å (P···C), 2.302 Å (P···N), and 3.325 Å (P···S). The O atoms of the EO$_2$-fragments interact with B, F or C$_\pi$ atoms.

The bonding analysis is complemented for **1-CO$_2$** by inspection of the frontier orbitals, see Figures S12–15. For **1**, the P atomic lone-pairs are described mainly by the HOMO and HOMO-1 (Figure S12). For **1-CO$_2$** (Figure S13), the donation of P atomic lone-pair density into the non-bonding LUMO of CO$_2$ (Figure S15) to form the P–C(O$_2$)–P interaction is described by the HOMO-5 molecular orbital, suggesting a stabilization of the corresponding orbital(s) by circa 0.047 Hartree (-122 kJ mol^{-1}). The remaining occupied frontier orbitals of **1-CO$_2$** are domi-

nated by ligand-based aromatic π-orbitals, with little to no CO$_2$-contributions. The LUMO + 1 and LUMO + 2 have recognizable CO$_2$-contributions as well, but are still dominated by the ligand system.

Conversion of CO$_2$ into methanol and water. In the last two sections we showed that following the concept of Frustrated Lewis Pairs (FLPs) light-atom molecules with particular numbers and relative orientations of Lewis acidic and basic sites, as well as (limited) structural flexibility, are capable of uptake and activation of small gaseous element oxides, such as CO$_2$, NO$_2$, and SO$_2$, and we showed the effects this activation has to the electronic bond characteristics of these molecules, making them prone to subsequent chemical conversions. The ultimate goal of course is the transformation of such hazardous and environmentally critical compounds into value added products, which can be fed back into industrial cycles. The majority of these issues are solved nowadays with heterogeneous catalysis on the large scale typically involving transition-metals and their oxides, however, the search for homogeneous, particular transition-metal free, alternatives remains relevant. Within this study we test the most promising candidate for CO$_2$ uptake, **1-CO$_2$**, against full reduction to give methanol and water, and we compare it to results obtained for the dicationic *Si$_2$P$_2$*-ligand system (**4**), which was used for N$_2$ activation in a previous study.[19] Since the latter involves the formation of strong Si–O bonds, which likely are hard to break in the final steps of releasing products, we use this system only as reference. In

ChemistrySelect

Research Article
doi.org/10.1002/slct.202301173

Chemistry
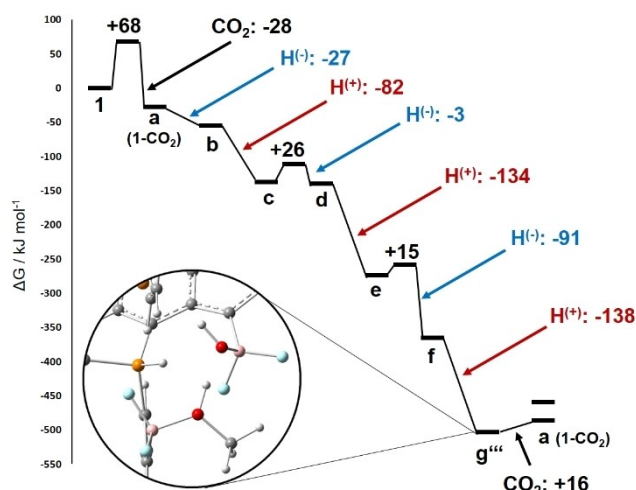Europe
European Chemical
Societies Publishing

order to limit the considerable computational efforts, we don't conduct a fully comprehensive study for both ligand systems, including all potential side reactions for each of the six reduction/protonation steps, many of which didn't converged after extended periods of time. Thus, we show explicitly only those electronic states, which provided the largest energetic gain and present only the "main route" towards the final products, so the results should rather be considered as a proof-of-concept study than a complete picture. All presented structures were fully converged. For the B_2P_2-ligand (**1**), frequency calculations were conducted on all structures to obtain ΔG-values (see Figures 5 and 6), for the considerably larger Si_2P_2-ligand, the discussion was restricted to ΔE. To get a more reasonable picture, we added an artificial penalty to ΔE which should compensate for three correction steps: 1. $\Delta E \rightarrow \Delta G$, 2. BSSE, 3. 1 atm $\rightarrow$ 1 M (see Figure S10). CO_2 uptake was thus "fined" with 100 kJ mol^{-1} (see discussion above), adding hydride with 30 kJ mol^{-1}, protonation with 10 kJ mol^{-1}, thereby resembling the values obtained for the B_2P_2-ligand. For schematic presentation of the CO_2-reduction cycle using **1**, see Figure 5, for molecular representations of both systems Figures S17 and S18.

A PES varying the $P_{central}\cdots CO_2$ distance in narrow steps was conducted for the Si_2P_2-ligand and accordingly refined for the B_2P_2-ligand to provide a detailed comparison of their CO_2-uptake capabilities, see Figure S20. Two conclusions can be

Figure 6. Gibbs Energy diagram of the proposed main route for CO_2-uptake, subsequent proton-balanced reduction (transfer of hydrogen equivalents), and final release of methanol and water, applying ligand system **1**. The transition-state for CO_2-adduct formation is 68 kJ mol^{-1} (Figure S4); potential energy scans indicate barriers of about 26 and 15 kJ mol^{-1} for the second and third reduction step, whereas the first reduction and all three protonation steps likely occur without any relevant kinetic barrier (Figure S19). For clarity, reductions steps are highlighted by blue arrows and text, whereas protonation steps are highlighted in red. The structure shows a zoom-in into the final electronic state g''', which carries a hydroxyl group, a methanol fragment, as well as a protonated P atom. Gentle heating under slightly elevated CO_2-pressure is supposed to release methanol and water and to provide the CO_2-adduct (**1-CO₂**), closing the catalytic cycle. The dark blue bar represents the enthalpy expense for the less favorable "extrusion pathway", i.e. release of methanol and water to re-form the free ligand **1**.

Figure 5. Proposed reaction scheme for CO_2-uptake, subsequent proton-balanced reduction (transfer of hydrogen equivalents), and final release of methanol and water, applying ligand system **1**. a) CO_2-adduct (**1-CO₂** or **1-a**); b) Adding hydride at the central C atom (**1-b**); c) Protonation at the free P atom (**1-c**); d) Adding second hydride at the central C atom (**1-d**); e) Protonation at the second P atom (**1-e**); f) Adding the third hydride at the central C atom, breaking a C–O bond (**1-f**) accompanied by proton move from P to O; g) Protonation at different sites to form the final state: g') Water and methoxyl, and one P–H, g'') Hydroxyl, methoxyl, and two P–H, g''') Hydroxyl, methanol, and one P–H.

drawn from this figure: first, the entry barrier for CO_2 to enter the active site of the Si_2P_2-ligand is likely twice as high as for the B_2P_2-ligand, in other words, more than 100 kJ mol^{-1} (a TS has not been calculated for Si_2P_2 because it serves only as reference system); second, CO_2-uptake is a multi-step procedure involving three different binding motifs for CO_2: a loosely associated molecule pair at about 5 Å, a pre-activation structure involving one Lewis acid and one Lewis base at about 3 Å (B_2P_2) or 3.5 Å (Si_2P_2), and the final EO_2-complexes involving both Lewis acidic and basic sites at about 2.5 Å or closer.

The first reaction of the CO_2-adducts unavoidably will be the reduction with hydride, as all attempts to protonate **1-a** ($=$ **1-CO₂**) or **4-a**, e.g. at the O atoms, failed. Due to the stronger activation in the dicationic system **4-a** compared to **1-a**, this step provides -53 kJ mol^{-1} (after penalty) for the former and -27 kJ mol^{-1} for the latter. In both cases, this reduction causes the disruption of the P–C bond opposite to the attack site, see parts a and b of Figures 5, S17, and S18. Already at step two, the reaction paths start to differ between both ligand systems. Whereas the somewhat expected "conservative" iterative reduction-protonation route was found to be the most likely path for **1**, thereby resembling the proton-coupled electron transfer (PCET) reactions in protein biochemistry, **4** follows another main route, which is: twofold reduction, protonation, reduction, twofold protonation. Consequently, we follow the CO_2RR in **1** first, then compare to **4**. Protonation of **1-b**

ChemistrySelect

Research Article
doi.org/10.1002/slct.202301173

Chemistry Europe
European Chemical
Societies Publishing

unavoidably happens at the now free P atom, see structure **1-c** in Figure 5 or S17. Further reduction towards **1-d** results in the formation of a diolate-like fragment ($^-B-O-CH_2-O-B^-$) and release of the second P atom, which is energetically not strongly favored. In contrast, the following protonation – again at the newly free P atom – is strongly favored (**1-e**), still more than protonation at an O atom (not shown). The third and final reduction is also strongly favored (**1-f**), as it finally breaks one C–O bond, resulting in the generation of a methoxyl ($-B-O-CH_3$) fragment on one side, whereas the remaining $-BO^-$ fragment drags away the proton of the adjacent P–H group to form a hydroxyl (B–OH). All attempts to reduce the $-BF_2$ groups to form $-BF_2H$ failed and can be excluded. Since there are several potential structural isomers possible after the third and final protonation step (**1-g**), the details of which are of relevance for the release of products and the possibility to close the catalytic cycle, we calculated three isomers: **1-g'** is protonated at the –OH group to pre-form water, the structure of which is stabilized by a O–H···O hydrogen bond between the hydroxyl and the methoxyl part; **1-g''** is protonated at the now again free P atom, which provides much less gain in ΔG; **1-g'''** is protonated at the $-OCH_3$ group, which also is stabilized by a O–H···O hydrogen bond and provides the highest enthalpic gain, so accordingly, we depict the electronic state **1-g'''** to be the main final state formally comprising the ligand system, a methanol, and a water molecule. The crucial point is now the release of the two products, methanol and water, to re-enter the proposed cycle. There are two ways, the extrusion pathway and the exchange pathway. Extrusion means, the products are released by (gentle) heating of the system to provide the free ligand, **1**. Taking this route comes with an expense of $\Delta G = 44.2 \text{ kJ mol}^{-1}$. Exchange means, the system is (gently) heated while bubbled with (slightly pressurized) CO_2 to provide the desired products and the CO_2-adduct **1-a**, which comes with an expense of only $\Delta G = 16.7 \text{ kJ mol}^{-1}$ and seems feasible. It has the additional advantage, that the cycle is one step smaller compared to the extrusion route. So far, the discussion of reducing CO_2 included only steady-state structures, thus reaction thermodynamics. In order to estimate reaction kinetics, relaxed PES were conducted for the three reduction steps with hydride by keeping the C···H$^{(-)}$ distances at fixed distances (Figure S19a), as these steps involve considerable structural modifications and change the number of electrons in the system. In contrast, the three protonation steps are found to occur without barrier (Figure S19b). The PES of the reduction steps reveals minor reaction barriers of less than 30 kJ mol^{-1}, thus, in an overall picture, it seems reasonable to perform the full chemical conversion of CO_2 into methanol and water using this ligand system. On the one hand, potential side reactions in the lab might limit the practical application. On the other hand, the system surely can be optimized by variation of Lewis acidic and basic sites, the spacer fragment, and the practical conditions (solvent, temperature) in the chemical laboratory. As mentioned in the DFT methodological section, the steady-state structures of the CO_2-reduction pathway were reoptimized at the higher B3PW91/6-311+G(2df,p) level of theory, fully resembling the trends obtained for the lower-level

calculations. Conserved trends were also found in previous studies on N_2[19] and CH_4.[22]

A brief look at the CO_2RR employing the Si_2P_2-ligand (**4**) unravels the same basic steps (Figure S18), despite the different order of events, which gives some confidence in the proposal of the "main routes". First and second reduction (**4-b**, **4-c**) result in the release of the P atoms and formation of a diolate-like fragment. Subsequent protonation occurs at a P atom (**4-d**). The third reduction (**4-e**) breaks one C–O bond generating a hydrogen bonding stabilized hydoxyl-methoxyl-fragment. The second protonation again takes place at a P atom (**4-f**). A difference to the B_2P_2-system (**1**) is found for the third and final protonation, which again occurs at a P atom (compare to state **1-g''** in Figure 5), but no efforts have been spent to find a **1-g'''** analogue of lower energy. The energetic/enthalpic expense of product release and exchange with CO_2 to re-form **4-a** is not clear, but a positive ΔE of 8 kJ mol^{-1} points towards a considerably endothermic process, making **1** superior over **4** for CO_2RR.

It is yet unclear how the corresponding reduction of NO_2 and SO_2 occurs, which has to be addressed in later studies.

Conclusions

Small molecule activation is essential to all forms of life and nature in the course of biologic evolution has developed highly task-specific three-dimensional organometallic structures (proteins and supportive molecules) to accomplish the required chemical conversions. Synthetic chemistry – supported by large-scale computational screenings on model systems – can reduce the scale and complexity and likely even can abstain from the use of transition-metal atoms to serve as electron-shuttle or -storage. Nevertheless, the key concepts of biochemical reactions – the use of one particular protein for each type of chemical conversions, the concept of the entatic state forcing the substrate molecules in to transition-state-like geometries within a structurally dynamic active site, and the charge-balancing proton-coupled electron transfers, also apply to the design of successful synthetic systems. The proposed tripodal *peri*-substituted compounds, which employ the concept of Frustrated Lewis Pairs (FLPs), exhibit a modular design facilitating target-specific variation of numbers and kinds of used Lewis acids and bases, as well as of the spacer molecules which define the dimensions of the void/binding pocket/active site. Limited structural flexibility guarantees structural and electronic accommodation of the ligand system *via* the subsequent reaction steps, which is not possible if a rigid system with fixed acid-base-distance is employed. Previous variations of the theme enabled the partial reduction of gaseous N_2 into NH_3, as well as the capture of noble gas atoms and methane; here, we show the potential application towards CO_2 reduction, and chemical conversion of hazardous gases such as NO_2 and SO_2. All proposed variations are principally accessible by means of synthetic chemistry, which is a basic demand within our screening approach.

ChemistrySelect

Research Article
doi.org/10.1002/slct.202301173

Chemistry Europe
European Chemical
Societies Publishing

Supporting Information Summary

Supporting information contains structural motifs including relative energies and relevant distances, PES diagrams, RSBI and MO figures, reaction schemes, as well as tables listing energies and enthalpies or RSBI-parameters.

Acknowledgements

Conflict of Interests

The authors declare no conflict of interest.

Data Availability Statement

The data that support the findings of this study are available from the corresponding author upon reasonable request.

[1] B. M. Hoffman, D. Lukoyanov, Z. Y. Yang, D. R. Dean, L. C. Seefeldt, *Chem. Rev.* **2014**, *114*, 4041–4062.

[2] A. M. Appel, J. E. Bercaw, A. B. Bocarsly, H. Dobbek, D. L. DuBois, M. Dupuis, J. G. Ferry, E. Fujita, R. Hille, P. J. A. Kenis, C. A. Kerfeld, R. H. Morris, C. H. F. Peden, A. R. Portis, S. W. Ragsdale, T. B. Rauchfuss, J. N. H. Reek, L. C. Seefeldt, R. K. Thauer, G. L. Waldrop, *Chem. Rev.* **2013**, *113*, 6621–6658.

[3] Q. Wang, K. Domen, *Chem. Rev.* **2020**, *120*, 919–985.

[4] J. Schneider, H. F. Jia, J. T. Muckerman, E. Fujita, *Chem. Soc. Rev.* **2012**, *41*, 2036–2051.

[5] T. A. Rokob, A. Hamza, A. Stirling, T. Soos, I. Papai, *Angew. Chem. Int. Ed.* **2008**, *47*, 2435–2438; *Angew. Chem.* **2008**, *120*, 2469–2472.

[6] D. W. Stephan, *Org. Biomol. Chem* **2008**, 10.1039/b802575B, 1535–1539.

[7] G. Menard, D. W. Stephan, *J. Am. Chem. Soc.* **2010**, *132*, 1796-+.

[8] D. W. Stephan, G. Erker, *Angew. Chem. Int. Ed.* **2010**, *49*, 46–76; *Angew. Chem.* **2010**, *122*, 50–81.

[9] S. Grimme, H. Kruse, L. Goerigk, G. Erker, *Angew. Chem. Int. Ed.* **2010**, *49*, 1402–1405; *Angew. Chem.* **2010**, *122*, 1444–1447.

[10] D. W. Stephan, *Accounts Chem Res* **2015**, *48*, 306–316.

[11] S. A. Weicker, D. W. Stephan, *Chem. Eur. J.* **2015**, *21*, 13027–13034.

[12] A. E. Ashley, A. L. Thompson, D. O'Hare, *Angew. Chem. Int. Ed.* **2009**, *48*, 9839–9843; *Angew. Chem.* **2009**, *121*, 10023–10027.

[13] C. M. Momming, E. Otten, G. Kehr, R. Frohlich, S. Grimme, D. W. Stephan, G. Erker, *Angew. Chem. Int. Ed.* **2009**, *48*, 6643–6646; *Angew. Chem.* **2009**, *121*, 6770–6773.

[14] M. A. Courtemanche, M. A. Legare, L. Maron, F. G. Fontaine, *J. Am. Chem. Soc.* **2013**, *135*, 9326–9329.

[15] M. A. Courtemanche, J. Larouche, M. A. Legare, W. H. Bi, L. Maron, F. G. Fontaine, *Organometallics* **2013**, *32*, 6804–6811.

[16] T. Wang, D. W. Stephan, *Chem. Eur. J.* **2014**, *20*, 3036–3039.

[17] M. A. Courtemanche, A. P. Pulis, E. Rochette, M. A. Legare, D. W. Stephan, F. G. Fontaine, *Chem. Commun.* **2015**, *51*, 9797–9800.

[18] P. Federmann, T. Bosse, S. Wolff, B. Cula, C. Herwig, C. Limberg, *Chem. Commun.* **2022**, *58*, 13451–13454.

[19] S. Mebs, J. Beckmann, *Phys. Chem. Chem. Phys.* **2022**, *24*, 20953–20967.

[20] S. Mebs, *ChemPhysChem* **2022**, *24*, e202200621.

[21] S. Mebs, J. Beckmann, *Phys. Chem. Chem. Phys.* **2022**, *24*, 20968–20979.

[22] S. Mebs, J. Beckmann, *Phys. Chem. Chem. Phys.* **2023**, *25*, 5656–5662.

[23] R. F. W. Bader, *B Am Phys Soc* **1977**, *22*, 305–306.

[24] R. F. W. Bader, T. T. Nguyendang, *Adv. Quantum Chem.* **1981**, *14*, 63–124.

[25] R. F. W. Bader, *Accounts Chem Res* **1985**, *18*, 9–15.

[26] E. R. Johnson, S. Keinan, P. Mori-Sanchez, J. Contreras-Garcia, A. J. Cohen, W. T. Yang, *J. Am. Chem. Soc.* **2010**, *132*, 6498–6506.

[27] M. Kohout, *Int. J. Quantum Chem.* **2004**, *97*, 651–658.

[28] A. D. Becke, *J. Chem. Phys.* **1993**, *98*, 1372–1377.

[29] J. P. Perdew, J. A. Chevary, S. H. Vosko, K. A. Jackson, M. R. Pederson, D. J. Singh, C. Fiolhais, *Phys. Rev. B* **1992**, *46*, 6671–6687.

[30] M. J. T. Frisch, G. W. Schlegel, H. B. Scuseria, G. E. Robb, M. A. Cheeseman, J. R. Scalmani, G. Barone, V. Petersson, G. A. Nakatsuji, H. Li, X. Caricato, M. Marenich, A. V. Bloino, J. Janesko, B. G. Gomperts, R. Mennucci, B. Hratchian, H. P. Ortiz, J. V. Izmaylov, A. F. Sonnenberg, J. L. Williams-Young, D. Ding, F. Lipparini, F. Egidi, F. Goings, J. Peng, B. Petrone, A. Henderson, T. Ranasinghe, D. Zakrzewski, V. G. Gao, J. Rega, N. Zheng, G. Liang, W. Hada, M. Ehara, M. Toyota, K. Fukuda, R. Hasegawa, J. Ishida, M. Nakajima, T. Honda, Y. Kitao, O. Nakai, H. Vreven, T. Throssell, K. Montgomery, J. A., Jr. Peralta, J. E. Ogliaro, F. Bearpark, M. J. Heyd, J. J. Brothers, E. N. Kudin, K. N. Staroverov, V. N. Keith, T. A. Kobayashi, R. Normand, J. Raghavachari, K. Rendell, A. P. Burant, J. C. Iyengar, S. S. Tomasi, J. Cossi, M. Millam, J. M. Klene, M. Adamo, C. Cammi, R. Ochterski, J. W. Martin, R. L. Morokuma, K. Farkas, O. Foresman, J. B. Fox, D. J., C.01 ed., Gaussian, Inc., Wallingford CT, **2016**.

[31] S. Grimme, *J. Comput. Chem.* **2006**, *27*, 1787–1799.

[32] S. Miertus, E. Scrocco, J. Tomasi, *Chem. Phys.* **1981**, *55*, 117–129.

[33] C. J. Cramer, *Essentials of Computational Chemistry: Theories and Models*, 2nd ed., Wiley & Sons Ltd, **2004**.

[34] F. Biegler-Konig, J. Schonbohm, D. Bayles, *J. Comput. Chem.* **2001**, *22*, 545–559.

[35] M. Kohout, *Vol. Radebeul*, 4.6 ed., **2015**.

[36] J. Contreras-Garcia, E. R. Johnson, S. Keinan, R. Chaudret, J. P. Piquemal, D. N. Beratan, W. T. Yang, *J. Chem. Theory Comput.* **2011**, *7*, 625–632.

[37] C. B. Hübschle, P. Luger, *J. Appl. Crystallogr.* **2006**, *39*, 901–904.

[38] P. Comba, *Coordin Chem Rev* **2000**, *200*, 217–245.

[39] J. Villa, M. Strajbl, T. M. Glennon, Y. Y. Sham, Z. T. Chu, A. Warshel, *P Natl Acad Sci USA* **2000**, *97*, 11899–11904.

[40] Y. Chen, S. Ye, L. Jiao, Y. Liang, D. K. Sinha-Mahapatra, J. W. Herndon, Z. X. Yu, *J. Am. Chem. Soc.* **2007**, *129*, 10773–10784.

[41] S. Raub, G. Jansen, *Theor. Chem. Acc.* **2001**, *106*, 223–232.

[42] S. Grabowsky, P. Luger, J. Buschmann, T. Schneider, T. Schirmeister, A. N. Sobolev, D. Jayatilaka, *Angew. Chem. Int. Ed.* **2012**, *51*, 6776–6779; *Angew. Chem.* **2012**, *124*, 6880–6884.